Full Length Article

Feasibility study of gas injection in low permeability reservoirs of Changqing oilfield

Ye Tian[a], Ozan Uzun[a], Yizi Shen[a], Zhengdong Lei[b], Jiangru Yuan[b], Jiaheng Chen[a,b], Hossein Kazemi[a], Yu-Shu Wu[a,*]

[a] Petroleum Engineering Department, Colorado School of Mines, Golden, CO 80401, USA
[b] Research Institute of Petroleum Exploration and Development, PetroChina, Beijing 10083, China

ARTICLE INFO

ABSTRACT

Changqing is the largest petroleum-producing field in China and one-third of its production is attributed to the formations with permeability lower than 1 mD. Based on the recent successes of gas injection pilots in North America, we investigated the feasibility of gas injection in the low permeability Chang 6_3 reservoir of Changqing. An eight-component fluid characterization, which fitted the measured PVT data, was used in a dual-porosity compositional model. A typical well pattern was selected for the simulation study. The key input parameters were adjusted to match the historical data. Huff-n-Puff using different gases shows that the richer the injected gas, the higher the oil production. C_3H_8 huff-n-puff achieves the best performance, increasing the cumulative oil production by a factor of 2.28 after 5 cycles, then followed by and the produced gas. CH_4 demonstrates a lower recovery factor (RF) than waterflood, because its minimum miscibility pressure is close to the maximum allowable injection pressure, i.e., the minimum horizontal stress. With the current well placement design where the producer is at the reservoir top, the miscible bank, which forms at the front of lean gas injection, will be displaced towards the reservoir bottom even out of the stimulated reservoir volume (SRV), undermining its performance. Rich gas is more compatible, as the miscible bank forms at the injection tail. Based on the fracture spacings from the published work, we could, for the first time, verify the technical feasibility of rich gas injection in Chang 6_3 following the presented compositional modeling framework.

1. Introduction

The Changqing oilfield located in the Ordos Basin is the largest oil and gas producing field in China and produced about 57 million tonnes of oil equivalent in 2019. The Changqing Oilfield Company, a subsidiary of PetroChina, first started its production in the 1970s from Jurassic formations with relatively high permeability ~10 mD [1,2]. In recent years, production from these formations became uneconomical; therefore, ultra-low permeability Triassic formations (~0.1 mD) have emerged as the main target of development [3].

Similarly with unconventional plays in North America, the initial high oil rate of the low permeability formations in Changqing often declines rapidly, resulting in a low recovery factor (RF) even with multistage fractured horizontal wells. In recent years, various injectants including low-salinity water [4], chemicals [5], nanofluid [6], foam [7], ketone solvent [8] and gas [9] have been proposed for improved/enhanced oil recovery (IOR/EOR) in low permeability unconventional oil reservoirs. Compared with the liquid , a gas injectant such as

hydrocarbon gas, CO_2, N_2, or their mixture often has a higher compressibility and a lower viscosity, leading to higher injectivity and energy supplement potentials for tight formations [10]. Moreover, injecting gas often causes less formation damage than liquid. The immiscible gas injection can supplement the reservoir pressure meanwhile the dissolution of injected gas can also swell the oil and reduce its viscosity [11]. For a miscible process, the interfacial tension (IFT) between injected gas and oil could be dramatically lowered, which would significantly increase the microscopic displacement efficiency in addition to the mechanism of an immiscible process [12]. Most importantly, gas injection especially huff-n-puff has demonstrated many successes in a series of pilots in North America [13–15]. Because of the reasons above, we investigated the feasibility of gas injection in the low permeability formation (Chang 6_3) of Changqing Oilfield using a compositional modeling framework, including reservoir fluid characterization, rock property evaluation, fracture network modeling, history matching and compositional simulation, which to the best of our knowledge, is the first time for this region.

1.1. Overview of Y284 Unit

By the end of 2017, the Y284 Unit [16] had 756 producers and their main producing layers lie in the third sub-member of the sixth member of the upper Triassic Yanchang formation also known as Chang 6_3, which contains green-greyish siltstones with dark grey mud intercalation [17]. The average air permeability without confining pressure is estimated as 0.38 mD. The main producing interval is Chang 6_3^1, which is a continuous sand body at the top of Chang 6_3 with the average thickness as 21.2 m, porosity as 12.1% and initial oil saturation as 55%.

The producers in the Y284 Unit can be classified into two categories: fractured vertical wells and fractured horizontal wells. Waterflood with 384 vertical injectors was implemented in this reservoir at the start of or even before production in order to compensate for the low initial reservoir pressure, which is a common practice in Changqing [18]. Most vertical wells are in the diamond inverted nine-spot pattern, with extended well spacing along the direction of maximum horizontal stress in order to delay water breakthrough along natural fractures and improve sweep efficiency as circled by the black long dash line in Fig. 1. The average oil production rate per vertical well was 1.47 m³/d and the average water-cut was 51.6% in 2017. The earliest production with vertical wells started in 2005. Horizontal wells with 6–8 fracture stages lie in the rectangular five-spot pattern as circled by the green short dash line in Fig. 1. The average oil rate per well for this five-spot pattern was 0.87 m³/d and the average water-cut was 64.1% in 2017 after 7 years of production. Horizontal wells with average 8 hydraulic fracture stages lie at the center of the rectangular seven-spot pattern as circled by the yellow line in Fig. 1. The average oil rate per well in the seven-spot pattern was 3.08 m³/d and the average water-cut was 32.5% as most of the wells in this pattern started production after 2012. The horizontal wells were mostly placed at the reservoir top but the vertical injectors were placed at the reservoir bottom, which was originally designed to improve the sweep efficiency of waterflood by gravity segregation. But still, the performance of waterflood in this unit is considered as unsatisfactory, resulting in a very low oil rate and lower than expected recovery factor. Early reservoir simulation studies predicted different
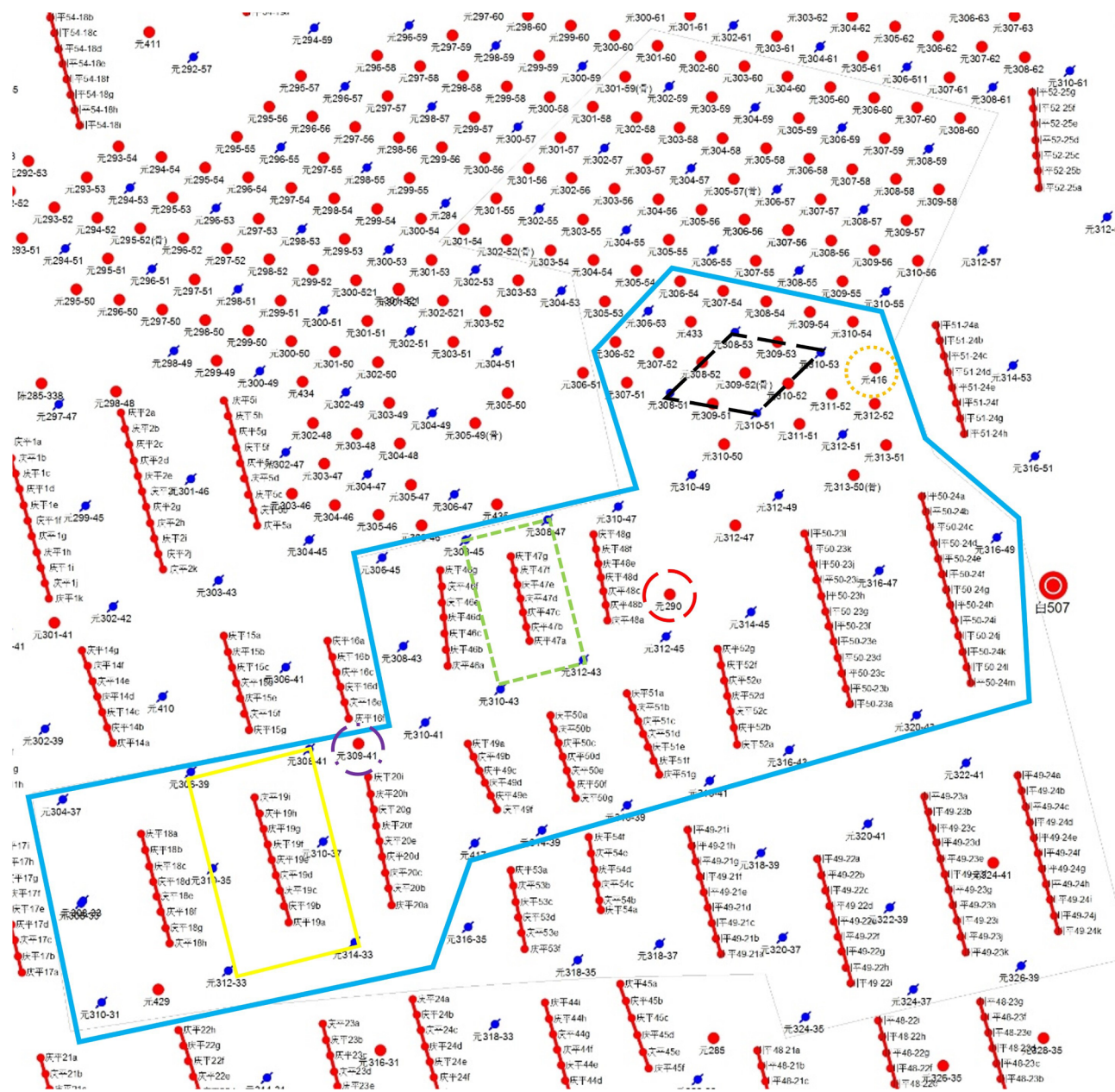

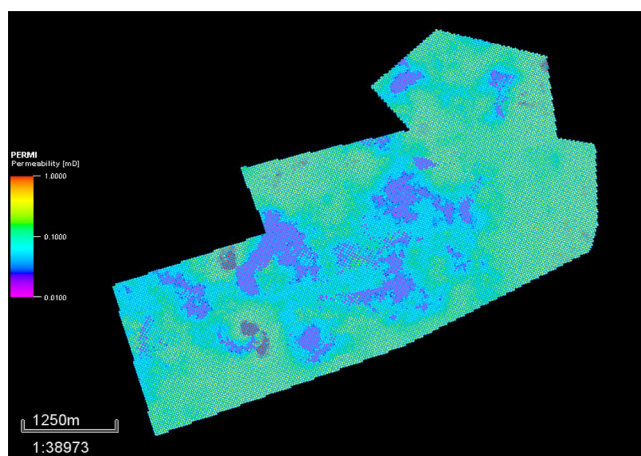**Fig. 1.** Boundaries of the pilot region within the Y284 Unit.

Fig. 2. The full-field model of the pilot region built by Hu [21].

ultimate recovery factors for example 10% [19], 15% [20] after waterflood in the horizontal-well-developed region. But the actual RF till 2017 was much lower than expected. Hence, IOR/EOR methods beyond waterflood is desired.

1.2. Pre-existing model of the pilot region

A pilot region which contained all three typical patterns as circled by the blue lines in Fig. 1, was hence selected by the operator for IOR/EOR pilot studies and was first investigated by Hu [21] using a black oil model as shown in Fig. 2. The grid size was 25 m in both I and J direction. And there were 15 vertical layers with the total thickness as 75 m. And the total grid number was 691,650 before refinement. The model was rotated 15 degrees counterclockwise in the IJ plane, making the I direction parallel to the direction of maximum horizontal stress as NE75°. Such rotation aimed at simplifying the fracture modeling as the local refinement was then only needed in the J direction. After grid refinements, the total grid number became 711,540. The initial reservoir pressure was 15.8 MPa and the temperature was 69.7 °C at the mid-depth of the reservoir.

The major issue with the previous black oil model was its poor history matching. With the total liquid rate as the history matching constraint, the oil rate was qualitatively matched. But there were apparent discrepancies with respect to the bottom hole pressure (BHP). The actual BHP (measured by a bottomhole pressure gauge from Aug 2016 to Sep 2016) was 5.2 MPa, much lower than the calculated BHP as 13.4 MPa from the black oil model as shown in Fig. 3. Reservoir properties including rock permeability, fracture conductivities, relative permeability curves should be carefully retuned to match the water cut and BHP during the waterflood to improve the model's reliability. Moreover, since the black oil model is no longer valid when the transport process is strongly composition-dependent during gas injection, it should be replaced by a compositional model to improve the simulation accuracy [10]. Hence, an equation-of-state (EOS) based compositional model was used to investigate the viability of gas injection in the Chang 6_3 formation of Changqing.

2. Compositional modeling

Running a full-field compositional model takes a significantly longer time than the black oil model due to the increased number of governing equations as well as costly phase equilibrium calculations. To reduce the computational cost, a typical well pattern containing the producer QP19 was subtracted from the pilot region (circled by the yellow solid line in Fig. 1 and compositionally modeled as shown in Fig. 4. Well QP19 was chosen because of the accessibility of production data. Although rate data were available for most wells in the pilot region, the

BHP was only measured by the downhole gauge for QP19 in the data file we received from the operator, which was a crucial input for history matching. Besides, QP19 is spatially closed to well Y309-41, where the reservoir fluid was sampled and analyzed as shown in Fig. 1.

Fig. 4 also illustrated the initial reservoir pressure before depletion, which together with initial water saturation and grid geometry were kept the same as the full-field model. There were 38,320 grids in the sub-model with 39 grids in the I direction, 61 grids in the J direction, and 15 grids in the K direction. There were seven wells in the sub-model including one fractured horizontal producer (QP19) and six water injectors (Y306-39, Y308-41, Y310-35, Y310-37, Y312-33, Y314-33). The water injection rate was proportionally scaled based on the well location, i.e., a factor of 1/4 for the injector at the corner (e.g., Y306-39) and a factor of 1/2 for the injector on the side (e.g., Y310-35). QP19 was perforated at the top of the reservoir and completed with 8 hydraulic fractures whose half-length ranged from 150 to 175 m in the I direction and height ranged from 8 to 16 m in the J direction. Water injectors injecting below the formation breakdown pressure were placed at the lower part of the reservoir, which was originally designed to improve the sweep efficiency of waterflood by gravity. In the following subsection, critical fluid and rock properties were meticulously re-calibrated and tuned based on the experimental results and production data in order to provide reliable inputs for the subsequent compositional simulation.

2.1. Reservoir fluid characterization

The reservoir fluid was sampled and tested in 2010 from producer Y309-41, whose location is circled by the purple long dash dot line in Fig. 1. Downhole sampling was carried out at a pressure of 13.501 MPa which was higher than the saturation pressure as 13.087 MPa. The fluid sample then underwent constant composition expansion (CCE) test, one-stage separator test and viscosity measurement at various pressure and constant reservoir temperature in a commercial laboratory. The overall molar composition of the fluid was listed in Table 1 with respect to 15 components. We then used a commercial software (CMG-WinProp) [22] to characterize the reservoir fluid system based on Peng-Robinson equation of state (EOS) [23] with its original mixing rule by [24].

For the practical compositional simulation purpose, we lumped the 15 components in the original PVT laboratory report into eight pseudo-components ($n_c = 8$) including CO_2, N_2, CH_4, C_2H_6, C_3H_8, C4-6, C7-10, C11+. C7+ was split into two pseudo components, i.e., C7-10 and C11+ based on the molar fraction of C7+ [25]. C4-6 was combined as a pseudo component but CH_4, C_2H_6, were listed as separated component due to the need to simulate gas injection. Because impurities like CO_2 or N_2 would affect the minimum miscibility pressure (MMP), they were also listed as an individual component. EOS parameters tuning is more of an art than an exact science. Our philosophy is that only the properties related to the pseudo-component are adjusted and detailed as follows,

Step 1: Split the C7+ fraction of the fluid into several pseudo-components based on its molar fraction[25].
Step 2: Tune the binary interaction coefficients (BIC) between pure components (especially CH_4) and pseudo-components to match the bubble point pressure.
Step 3: Adjust the critical properties and acentric factors of pseudo-components to match the ROV data from the CCE test as shown in Fig. 5.
Step 4: Tune the volume shift parameters [26] of pseudo-components to match the density data as shown in Fig. 6.
Step 5: Adjust parameters in the Jossi-Stiel-Thodos correlation [27] including critical volume, mixing rule exponent, and polynomial coefficients to match oil viscosities as shown in Fig. 7.
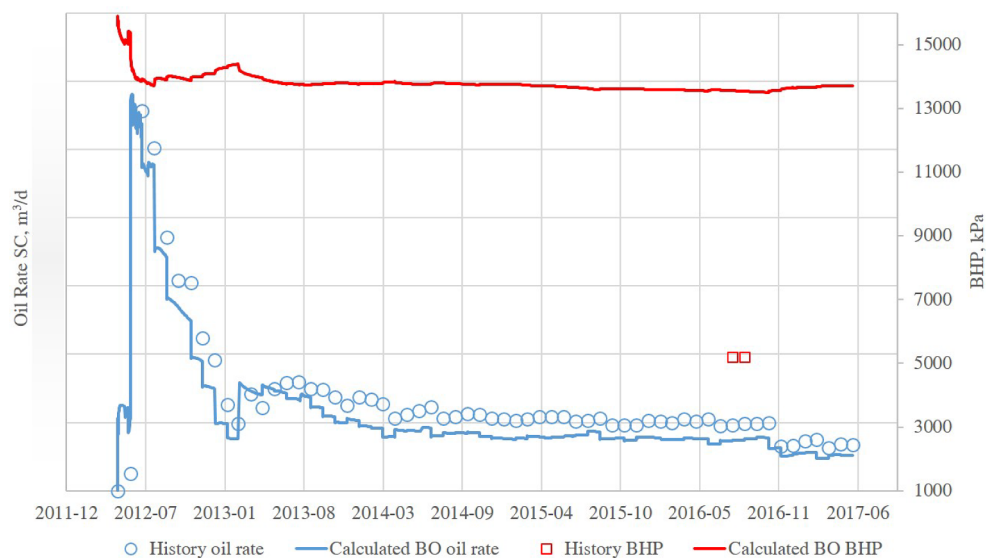
Fig. 3. Poor history-matching performance of Well QP19 by the previous black oil model by Hu [21].

It is worth mentioning that changing the critical temperature and critical pressure of pseudo-components will lead to mismatch of the saturation pressure. Hence, step 2–4 will be iteratively repeated until a satisfactory match is obtained for all the data considered. Generally, we desire a good match on the saturation pressure but could tolerate some errors regarding ROV or density.

The thermodynamic properties of the eight components after tuning are summarized in Table 2. Unlike the original form of volume translation by [26], the constant volume shift parameters in WinProp are dimensionless as shown in Table 2, following the modified expression by Jhaveri and Youngren (1988) [28]. The binary interaction coefficients after tuning are listed in Table 3. The binary interaction coefficients between any two pure components e.g., BIC between CH_4 and C_2H_6 were not tuned and default values from the WinProp library were used. The binary interaction coefficients between CO_2 (or N_2) and a pseudo-component e.g., BIC between CO_2 and C11+ might not be that reliable for modeling CO_2 (or N_2) injection due to its low molar fraction. We will be able to update the values as well as obtain a more accurate fluid model for gas injection if swelling tests, or slim tube tests are completed in the future.

The calculated gas-oil ratio at the bubble point is $120.10 \, m^3/m^3$, close to the measured value as $120.12 \, m^3/m^3$ at the stock-tank conditions of 20 °C and 101.325 kPa. The calculated stock-tank oil density for oil is $832.5 \, kg/m^3$ matching the experimental value as $832.5 \, kg/m^3$. The
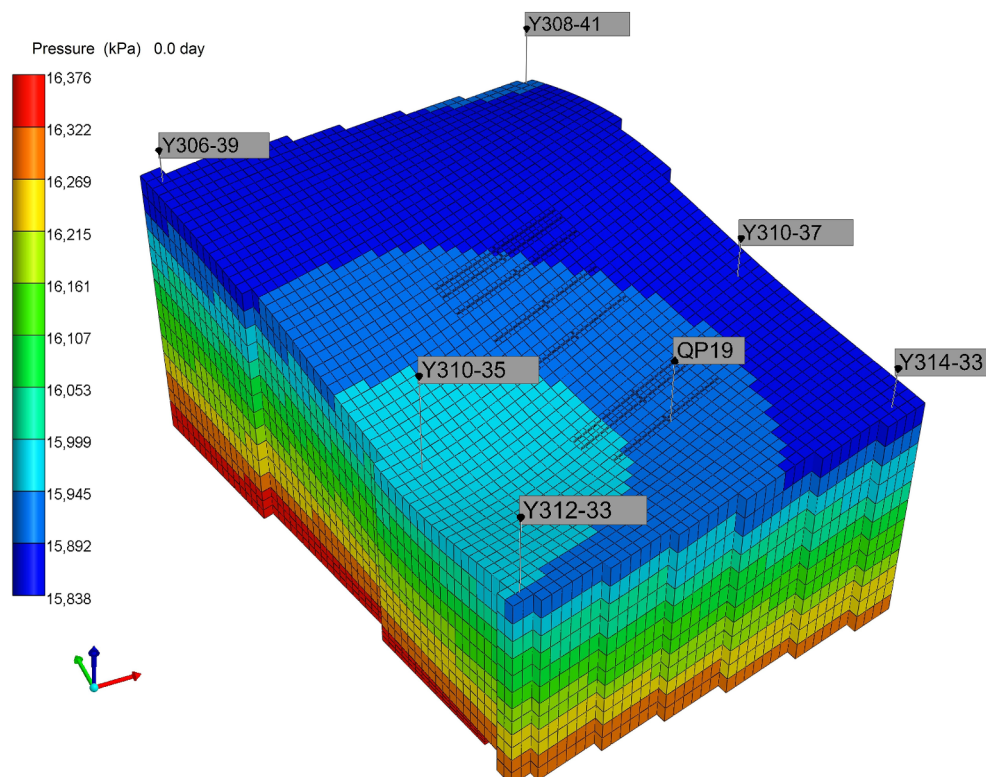

Fig. 4. A typical well pattern subtracted from the full-field model.

Table 1
Overall composition of the reservoir fluid.

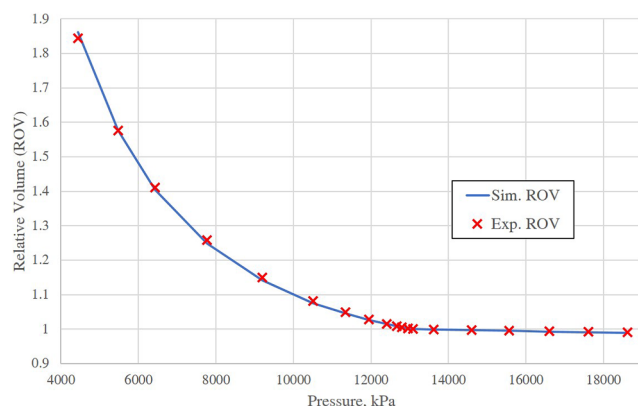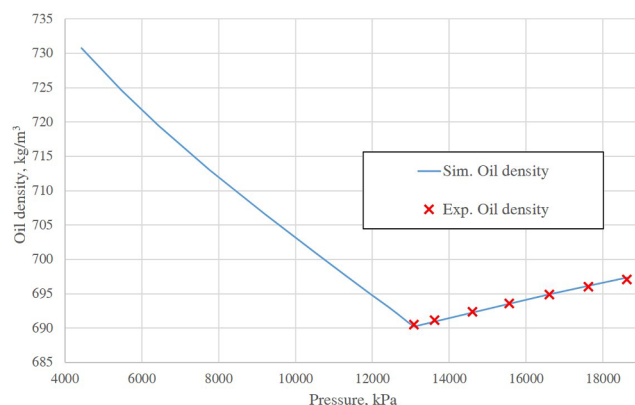| Component	N_2	CO_2	C1	C2	C3	iC4	nC4	iC5	nC5	C6	C7	C8	C9	C10	C11+
Molar fraction, %	0.75	0.12	31.72	8.35	9.70	1.49	4.62	1.62	2.25	2.84	3.24	4.49	2.88	2.25	23.67

Fig. 5. Matched relative volume.
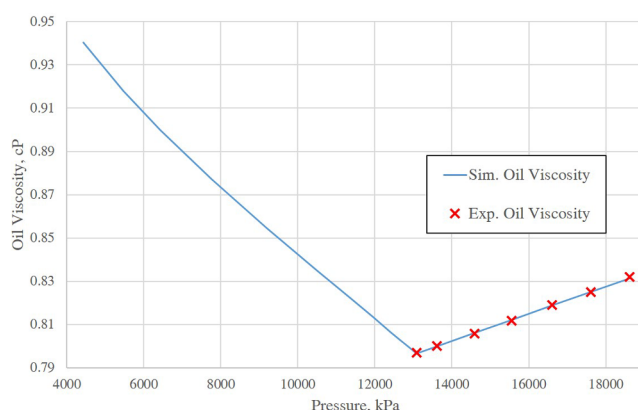

Fig. 6. Matched oil density.

Fig. 7. Matched oil viscosity.

calculated phase diagram based on the above fluid characterization is shown in Fig. 8.

2.2. Experimental evaluation of rock properties

The average air permeability without confining pressure was estimated as 0.38 mD, which was used in benchmarking the geological

model as well as the previous black oil models, making simulated BHP much higher than the actual BHP, as shown in Fig. 3. Hence, we re-characterized the rock porosity and permeability with two core plugs from well Y416 whose location is circled by the orange short dot line in Fig. 1. The length of core #1 is 1.237 in (3.142 cm) and its diameter is 1.480 in (3.759 cm). The length of core #2 is 1.455 in (3.696 cm) and its diameter is 1.482 in (3.764 cm). The cores were first cleaned by solvents (toluene, chloroform, and methanol sequentially) in a Soxhlet extractor and then dried in an oven.

Then an automated unsteady-state permeability and porosity measurement instrument (Core Lab CMS-300) was used to measure the permeability with nitrogen and porosity with helium because of its low adsorption volume. The instrument (CMS-300) uses an integrated form of the combined Darcy, Klinkenberg and Forchheimer equations to accurately determine the sample permeability under different confining stresses [29]. The confining stress was gradually increased first (loading) and then reduced again (unloading). For a specific confining stress, the instrument makes several measurements while reducing the pore pressure to obtain different permeabilities. These data points at different pore pressure are used to correct the slippage effect. The final output is hence the intrinsic rock permeability which excludes the Klinkenberg slippage effect. Both cores were tested at room temperature (20 ± 2 °C) and the results are summarized in Table 4 and Table 5 respectively. The porosity values from both cores are close to the initial average value of 12.1%. But the permeability measured under confining stress is two orders of magnitude smaller than the initial estimated value as 0.38 mD, which might explain the discrepancy between measured and simulated BHP in the previous model. Hence in the compositional submodel, a permeability multiplier as 0.01 was initially used for the history matching.

The unloading curves (lower two curves) are less stress-dependent than the loading curves (upper two curves) as shown in Fig. 9. It was discussed by Zhu et al. [30] that the first unloading process seems to better capture the stress-dependent behaviors especially for permeability than the first loading curve. Also, the hysteresis between loading and unloading curves will reduce and eventually vanish with more loading cycles [31]. Hence the unloading curve was used.

2.3. Mineralogical characterization

Eight samples from well Y416 (the same well where two core samples were measured for permeability and porosity) were analyzed using an automated SEM (TESCAN-VEGA-3 Model LMU) to determine their mineralogy and the analysis was initiated using the control program TIMA (TESCAN Integrated Mineral Analyzer). Four energy dispersive X-ray (EDX) spectrometers acquired spectra with a beam stepping interval (i.e., the spacing between acquisition points) of 1 μm, an accelerating voltage of 25 keV, and a beam intensity of 14. Interactions between the beam and the sample were modeled through Monte Carlo simulation. The EDX spectra were compared with spectra held in a look-up table allowing an assignment to be made of a component at each acquisition point. The assignment makes no distinction between mineral species and amorphous grains of similar composition. Results were output by the TIMA software as a spreadsheet giving the area fraction of each mineral component. The minerals were grouped appropriately and the mineral compositions for eight core samples were presented in Fig. 10. The average mineral composition is 31.8% plagioclase feldspar, 24.7% quartz, 10.6% chlorite-chamosite, 10.4% orthoclase feldspar, 8.2% calcite, 5.5% muscovite/illite, 3.7% dolomite

Table 2
Thermodynamic properties of the eight components.

Component	Molar fraction, %	Pc, atm	Tc, K	Acentric factor	MW, g/mol	Volume shift
CO_2	0.12	72.80	304.20	0.225	44.01	0
N_2	0.75	33.50	126.20	0.040	28.01	0
CH_4	31.72	45.40	190.60	0.009	16.04	0
C_2H_6	8.35	48.20	305.40	0.098	30.07	0
C_3H_8	9.70	41.90	369.80	0.152	44.10	0
C4-6	12.82	29.03	457.53	0.173	68.58	0
C7-10	12.86	21.87	463.77	0.354	118.75	−0.86963162
C11+	23.67	13.40	593.72	1.975	401.94	0.23767533

and others. The dominant fraction of feldspar and quartz and the minor fraction of calcite would imply a water-wet rock surface [32,33].

2.4. Relative permeability and capillary pressure

The water-oil relative permeability curves for the matrix were based on the published data [17] and its endpoint values were calibrated during history matching as shown in Fig. 11. The maximum krw in Fig. 11a is 0.18 and the saturation of equal oil and water relative permeabilities is 0.66 significantly higher than 0.5, which represent the typical characteristics of a water-wet system and are also consistent with the mineralogical analysis. Since the liquid-gas relative permeability curves were not available for this region, a hypothetical curve as shown in Fig. 11b was used based on the data from published studies [10]. The X-shape relative permeability curves were used for the multiphase flow in fracture networks by assuming minimal residual saturations and negligible capillary pressure as shown in Fig. 12.

The capillary pressure curve between air and mercury was available based on the experimental results of mercury injection from a previous study [17]. The water-oil capillary curve was obtained by converting the mercury-air curve using the Leverett J-function. For example, to convert the mercury-air curve into the water-oil curve, we have,

$$P_{cow} = P_{cHg-air} \left(\frac{\gamma_{ow} \cos\theta_{ow}}{\gamma_{Hg-air} \cos\theta_{Hg-air}} \right) \tag{1}$$

The drainage curve between water and oil as shown in Fig. 13 was used to initialize the water saturation at the beginning of the simulation.

Currently, we are using the core flood and centrifuge to obtain a better characterization of rock-fluid data, such as relative permeability and capillary pressure curves. But for now, the data tuned after history matching will be used in this preliminary feasibility study.

2.5. Modeling of fracture network

To effectively model fracture networks, different approaches have been proposed, includingthe discrete fracture network model (DFN), the embedded discrete fracture model (EDFM), and continuum approaches, such as the dual-porosity or Multiple INteracting Continua (MINC). In this study, we choose the combination of dual-porosity model and local grid refinement (LGR) due to the usage of a commercial simulator (CMG-GEM) [34]. Hydraulic fractures (HF) were modeled explicitly by LGR, and the grid containing HF has a width of 0.61 m, much larger than the actual width of HF as 0.002 m. The grid effective permeability is scaled accordingly to maintain the same fracture conductivity as specified [34]. For example, the grid block effective permeability for the propped HF is 98.4 mD, which is the propped HF's conductivity (60 mD·m) divided by the grid width (0.61 m). The natural fracture development for Chang 6_3 was well characterized in early studies [35–37]. Despite the low initial oil rate for vertical wells, the fracture density was high and fracture spacing was small as summarized in Table 6. In this study, natural fractures (NF) were modeled using the dual-porosity approach with fracture spacing set as 0.6 m in our base case. The effective natural fracture porosity was set as 0.001 to minimize the error introduced to pore volume after artificially adding fracture media into the previous single-porosity model. And the intrinsic permeability of natural fracture was initialized as 10 mD, resulting in an effective NF permeability as 0.01 mD.

2.6. History matching

The matching philosophy is to adjust a minimal number of parameters to fit the production data of well QP19. In order to match the BHP measured as 5.2 MPa from Aug 2016 to Sep 2016, the effective permeability of natural fractures was tuned to be 0.015 mD and the hydraulic fracture conductivity was adjusted from 60 mD·m to 64 mD·m. During the history matching, the matrix permeability multiplier was initialized as 0.01 based on the above mentioned experimental studies, but adjusting from 0.01 to 0.001 did not make significant impacts on simulation results, hence the initial value of 0.01 was retained.

To match the water cut, the relative permeability to water at residual oil saturation was reduced from 0.30 to 0.18. Despite mismatching oil rates at the early time of production (possibly due to unknown operational constraints), the history-matching performance as shown in Fig. 14 was significantly improved compared with the previous black oil model as shown in Fig. 3, especially at the late time which is more influential on the subsequent gas huff-n-puff operations.

Table 3
Binary interaction coefficients after tuning.

| Component	CO_2	N_2	CH_4	C_2H_6	C_3H_8	C4-6	C7-10	C11+
CO_2	0	0	0.105	0.13	0.125	0.115	0.2	0.2
N_2	0	0	0.025	0.01	0.09	0.11	0.11	0.18
CH_4	0.105	0.025	0	2.69E−03	8.54E−03	8.71E−03	1.93E−02	4.05E−02
C_2H_6	0.13	0.01	2.69E−03	0	1.66E−03	4.62E−03	1.46E−02	3.75E−02
C_3H_8	0.125	0.09	8.54E−03	1.66E−03	0	1.37E−03	8.11E−03	2.69E−02
C4-6	0.115	0.11	8.71E−03	4.62E−03	1.37E−03	0	4.06E−03	2.33E−02
C7-10	0.2	0.11	1.93E−02	1.46E−02	8.11E−03	4.06E−03	0	8.12E−03
C11+	0.2	0.18	4.05E−02	3.75E−02	2.69E−02	2.33E−02	8.12E−03	0
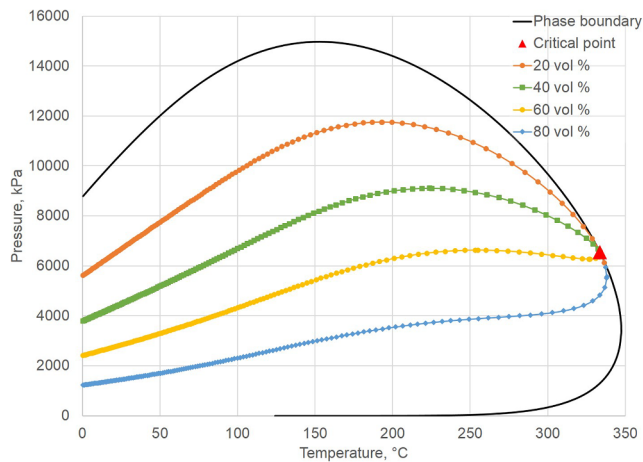
Fig. 8. Calculated phase diagram of the reservoir fluid.

Table 4
Permeability and porosity measured at different confining stress for core #1.

Net confining stress, psi	Net confining stress, kPa	Porosity, %	Permeability, 10^{-3} mD
788.7	5438	12.30	2.03
1047.4	7222	12.18	1.70
1514.7	10443	12.05	1.34
1512.4	10428	12.02	1.33
1106.1	7626	12.10	1.45
857.1	5909	12.16	1.55

Table 5
Permeability and porosity measured at different confining stress for core #2.

Net confining stress, psi	Net confining stress, kPa	Porosity, %	Permeability, 10^{-3} mD
735.8	5073	13.64	6.22
985.8	6797	14.12	5.40
1472.3	10151	14.16	4.05
1550.5	10690	14.17	3.91
1103.7	7610	14.19	4.28
813.2	5607	14.30	4.69

3. Sensitivity analysis

Unless noted otherwise, the huff-n-puff cases below employed a scheme consisting of 50-day injection, 10-day soaking, and 300-day production. The maximum injection BHP was set as 30 MPa unless specified otherwise, as the minimum horizontal stress was estimated as 31.5 MPa from well Y290 which is circled by the red long dash line in Fig. 1. The minimum production BHP was set as 5.2 MPa which was the actual value recorded from well QP19.

3.1. Compositional effect of the injected gas

The composition of the injected gas is a key factor to the performance of huff-n-puff, which is one of the reasons using the compositional model rather than the black oil model to study gas injection. Hence, we simulated the scenarios with different injectants, including CH_4, the produced gas (with its composition from the separator test), C_2H_6, and C_3H_8. The composition of different injectant is detailed in Table 7. The MMP between each injectant and the reservoir oil was estimated by the multiple mixing cell method in WinProp. Due to the lack of data from the slim-tube or swelling test, its value might subject to inaccuracy. But its general trend qualitatively matched our expectation, i.e., the richer the gas, the lower the MMP.

The compositional effect on the daily oil rate was shown in Fig. 15. CH_4 will only enhance oil production in the first huff-n-puff cycle. In the long term, its oil recovery was even lower compared with the waterflood scenario as shown in Fig. 16. Injecting C_3H_8 achieved the best performance, increasing the cumulative oil production on the basis of waterflood by a factor of 2.28 after 5 cycles, then followed by C_2H_6 as 1.34, produced gas as 1.08. The improvement factor as shown on the right side of Fig. 16, was calculated by dividing the cumulative C11+ production in moles after gas injection over the cumulative C11+ production in moles after waterflood. More generally, the improvement factor can be defined as the ratio of the cumulative oil production by an IOR/EOR method (gas huff-n-puff in this case) to the cumulative oil production following the original production scheme (waterflood in this case). This concept is more applicable in unconventional reservoirs [14,15], as most of the oil in place outside SRV is not accessible, making the recovery factor in the traditional sense very small. A richer mixture (i.e. with a higher molar fraction of intermediate component) will lead to a higher oil RF. Though C_3H_8 has the same value of intermediate fraction with C_2H_6, injecting C_3H_8 will still have a higher oil rate due to its lower MMP with the reservoir fluid than C_2H_6. Though injecting rich
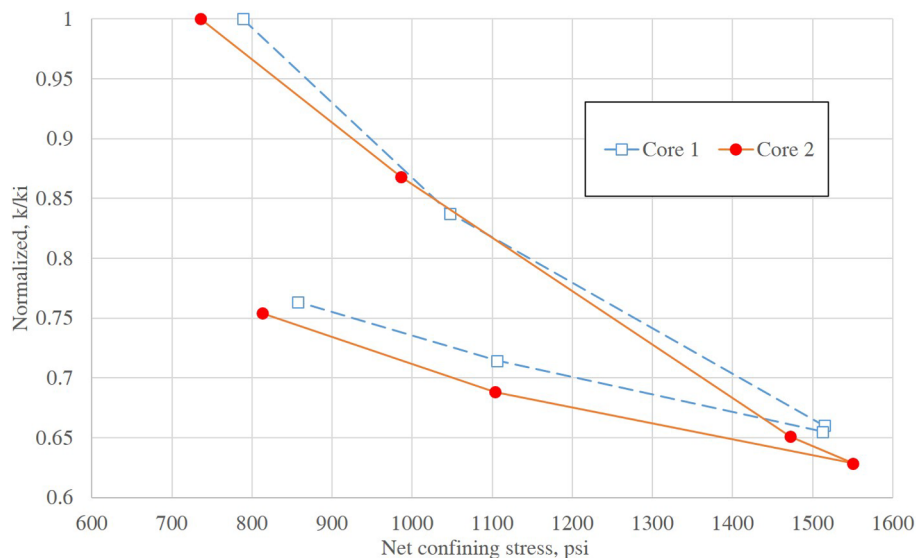

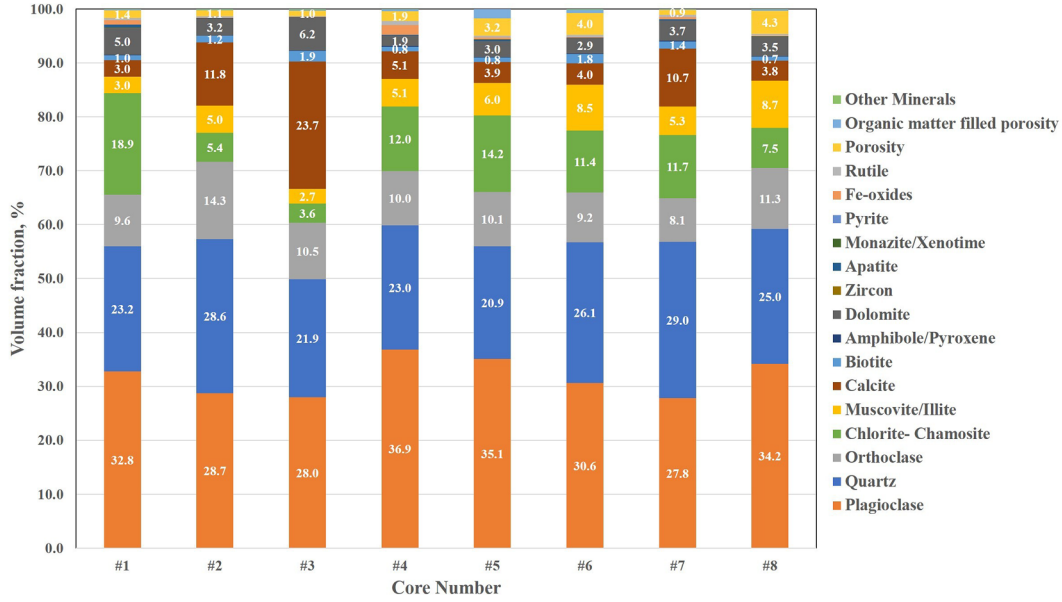**Fig. 9.** Stress-dependent permeability curves measured from cores.

Fig. 10. Mineralogy analysis for 8 cores from Well Y416.

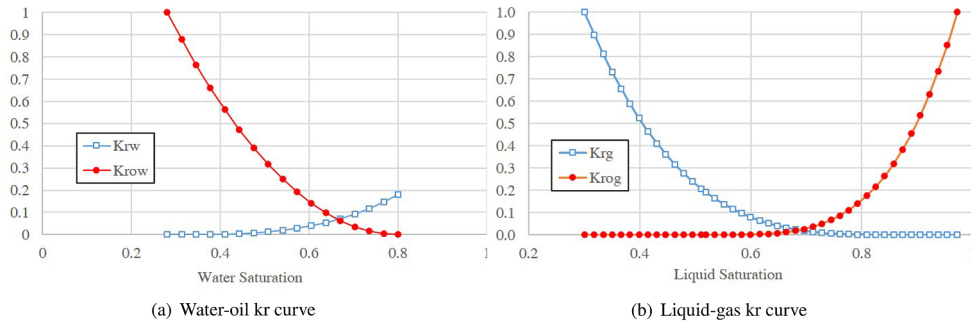(a) Water-oil kr curve   (b) Liquid-gas kr curve

Fig. 11. The relative permeability curve for the matrix.

gas (C_3H_8 or C_2H_6) might result in a higher technical recovery factor compared with leaner gas, its economics might not be feasible. Hence, we proposed to mix the produced gas with either C_2H_6 or C_3H_8 to lower the gas cost. For example, with a mixing ratio of 60% C_3H_8 and 40% produced gas, we could still improve the cumulative C11 + production by a factor of 1.57 compared with the waterflood base case, which was also higher than C_2H_6 injection as shown in Fig. 16.

To better compare the compositional effect between lean gas and rich gas injection, we can plot the map of calculated IFT in the J-K plane (e.g., Fig. 17) with the unit of both y and z axis in m. Fig. 17 also visualized the trajectory of well QP19 as well as the local grid refinements near the eight hydraulic fractures near the reservoir top. The interfacial tension between oil and gas phase σ_{og} is calculated as [38],

$$\sigma_{og}^{1/4} = \sum_{1}^{n_c} \chi_i (\rho_o x_i - \rho_g y_i)$$

(2)

where the parachor of a component χ_i uses the CMG's default values; the molar fraction of component i in the liquid phase x_i, the molar fraction of component i in the vapor phase y_i, and the density of oil ρ_o and gas ρ_g are all from the EOS calculation. At the end of primary depletion, the red region shown in Fig. 17 denotes the two-phase girds, where the matrix pressure is below the saturation pressure.

At the end of lean gas injection (CH_4), some of the red region turns blue again due to re-pressurization as shown in Fig. 18. Though the maximum injection BHP as 30 MPa was slightly above the MMP of CH_4 as 27 MPa, the actual pore pressure in most matrix grids are still lower
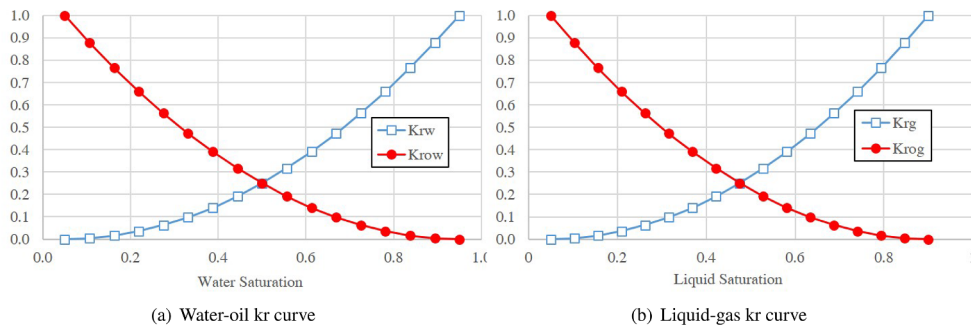

(a) Water-oil kr curve   (b) Liquid-gas kr curve

Fig. 12. The relative permeability curve for the fracture.
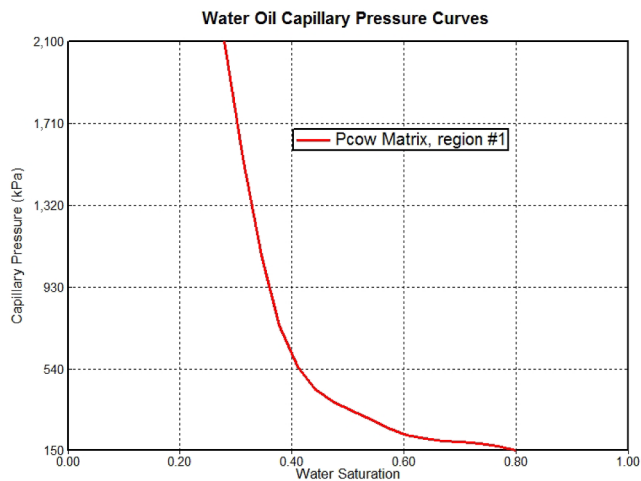
Fig. 13. Water–oil capillary pressure curve for the matrix.

Table 6
Natural fracture spacing from a publish study [36].

Well Name	NF spacing, m	Initial oil rate, m³/d
Y284	0.3	1.79
Y414	0.4	3.41
Y286	0.5	0.56
Y411	0.7	0.23
Y287	1.3	0.47
Y293	1.4	1.32
Y285	3.3	1.71
Y410	3.3	0.00
Y295	4.3	0.67
Y290	7.7	0.92

than the MMP due to the pressure losses when gas permeating the tight matrix. The IFT is reduced but not to zero as the miscibility is still not achieved. In addition, the injected gas from the reservoir top will displace the oil towards the reservoir bottom even out of the SRV, making its oil recovery even lower compared with the waterflood base case as discussed earlier.

At the end of produced gas injection (which can still be treated as lean gas though richer than CH_4), more red region becomes blue due to a lower saturation pressure with more intermediate components

injected with the produced gas as shown in Fig. 19. But the color transition in some grids are due to the archived miscibility, for example, the grid circled by the purple line. Above it, though the gas is very rich, the IFT is still greater than zero even with a high pressure, denoting a two-phase system passing the dew-point line. Two grids below the circled grid is a two-phase system (more like the original black oil system) passing the bubble-point line. The grid circled by the purple line hence denotes the transition between them, where miscibility is achieved. It can be seen that the circled grid is away from the injection points at the reservoir top but closer to the leading edge of the injection front which proves that the miscible bank is being pushed towards the reservoir bottom, even out of the SRV, undermining the huff-n-puff performance. Besides, the miscible oil bank even if formed during the injection will not be produced efficiently as it might be far away from the wellbore or even return to immiscibility due to pressure drop during the production, making its oil RF only slightly higher than the water-flood scenario.

The placement of producer QP19 at the reservoir top was initially designed to improve the sweep efficiency for waterflood by gravity, with water injectors perforated at the reservoir bottom. Rich gas injection is hence more compatible with the current well placement, because its miscible bank emerges at the injection point as shown in Fig. 20 instead of at the injection front for the lean gas scenario. The one-phase grids at the reservoir top could be the result of the first contact miscibility in addition to the multiple contact miscibility, which could also explain the higher oil increment of rich gas injection than lean gas.

3.2. Gas injection pressure

The BHP of the injection period is another important parameter influencing huff-n-puff performance. Often, the maximum BHP should be lower than the minimum horizontal stress to avoid undesired fracture propagation [15] or possible gas channeling. Hence, we simulated three different maximum BHP for the injection period i.e., 20 MPa, 25 MPa, and 30 MPa. For example, during C_2H_6 injection, a higher injection pressure would lead to a higher cumulative oil production as shown in Fig. 21. This was consistent with the experimental studies [12,39]. But still injecting C_2H_6 at 30 MPa could not outperform the injection of C_3H_8 at 20 MPa. When injecting below 25 MPa, C_2H_6 would not lead to significant improvement compared with the waterflood base scenario. The improvement factor for produced gas injection at 30 MPa as 1.08 is higher than the improvement factor of C_2H_6 injection at 25 MPa as 1.02, which is because the leaner composition of produced
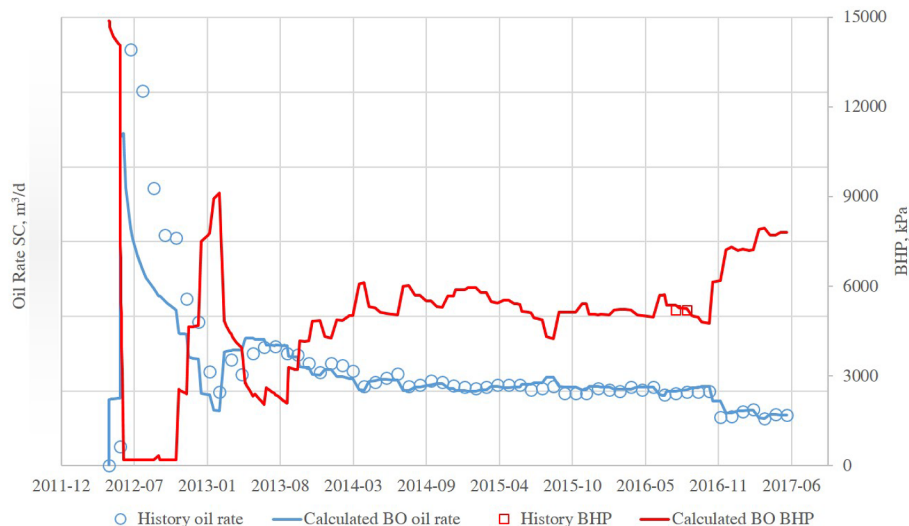

Fig. 14. Improved history-matching performance of Well QP19 by the current model.

Table 7
Composition of the injected gas.

	Light			Intermediate			Heavy		MMP, MPa
	CO_2	N_2	CH_4	C_2H_6	C_3H_8	C4-6	C7-10	C11+	
CH_4	0%	0%	100%	0%	0%	0%	0%	0%	27
		100%			0%			0%	
Produced gas	0.20%	1.30%	55.40%	14.30%	15.60%	12.50%	0.60%	0.00%	14.2
		57.00%			42.40%			0.60%	
C_2H_6	0%	0%	0%	100%	0%	0%	0%	0%	6.9
		0%			100%			0%	
C_3H_8	0%	0%	0%	0%	100%	0%	0%	0%	3.5
		0%			100%			0%	

gas was compensated by a higher injection pressure when the richness difference of two injectants is not too large.

3.3. Duration of the huff-n-puff stage

The duration of gas injection might affect the recovery factor. The huff-n-puff case above employed a scheme consisting of 50-day injection, 10-day soaking, and 300-day production. We then simulated different cases with 20-day, 70-day, 80-day, 90-day, and 110-day injection while maintaining the same soaking time and cycle duration constant as 360 days e.g., 80-day injection, 10-day soaking, and 270-day production. The simulation for 8 cycles shows that the cumulative C11+ production increased with injection time at first, but then the trend line would reach a plateau where increasing injection time would no longer lead to further improvement as shown in Fig. 22. For C_2H_6 huff-n-puff at 30 MPa, the critical injection time was found to be 80 days. Similarly, we investigated cases with different soaking time. The injection time was set the same as 80 days. The duration for one cycle was maintained the same as 360 days, e.g., 80-day injection 30-day soaking, 250-day production. The cumulative production has a relatively smaller dependence on soaking time compared with injection duration. At first, a longer soaking time would lead to a higher C11+ recovery, then a maximum would be achieved around 7-day as shown in Fig. 23. After that, a longer soaking time would not increase but reduce C11+ recovery factor due to the possibility of losing miscibility or displacing the reservoir oil out of the SRV. For C_2H_6 huff-n-puff at 30 MPa, the improvement factor would peak after 7 days of soaking.

During soaking, the main mechanism is the mass transfer between the injected gas and the in situ oil which enables the subsequent mechanisms such as oil swelling, oil viscosity reduction, IFT reduction [5]. Advection dominates the transport in the fractures, while diffusion might be important for the matrix-fracture or matrix-matrix transport [41]. In this study, we chose not to include the diffusion in the simulation for the following reasons. First, it would introduce additional uncertainties to history matching without having a rigorous multi-component diffusion model as an option in the current simulator. Most commercial simulators implemented the Fickian type diffusion model which neglects the cross-diffusion terms for a multicomponent system and hence is inconsistent with the equilibrium thermodynamics [40]. Secondly, with a more rigorous implementation of Stefan-Maxwell type diffusion theory in the in-house simulator, Hoteit and Firoozabadi [42] found that the effect of diffusion is minor when the injection pressure is above MMP as the determinant of the diffusion coefficient matrix is zero at the critical point (i.e., multiple contact miscibility). In our case, the injection pressure was 30 MPa, higher than the MMP of all the injectant in this study, which might to some extent justify neglecting diffusion.

3.4. Effect of fracture spacing

The properties of fracture network are known to influence the performance of reservoirs. Due to the inherent uncertainty regarding natural fracture spacing, different values were investigated. Based on Table 6, we then investigated NF spacing as 8 m, ∞ m (no fractures, single-porosity model). Using a different fracture spacing other than the base case as 0.6 m would require re-history-matching the production data. We mainly re-tuned the natural fracture permeability to re-match the BHP. The water-oil relative permeability endpoint also was slightly
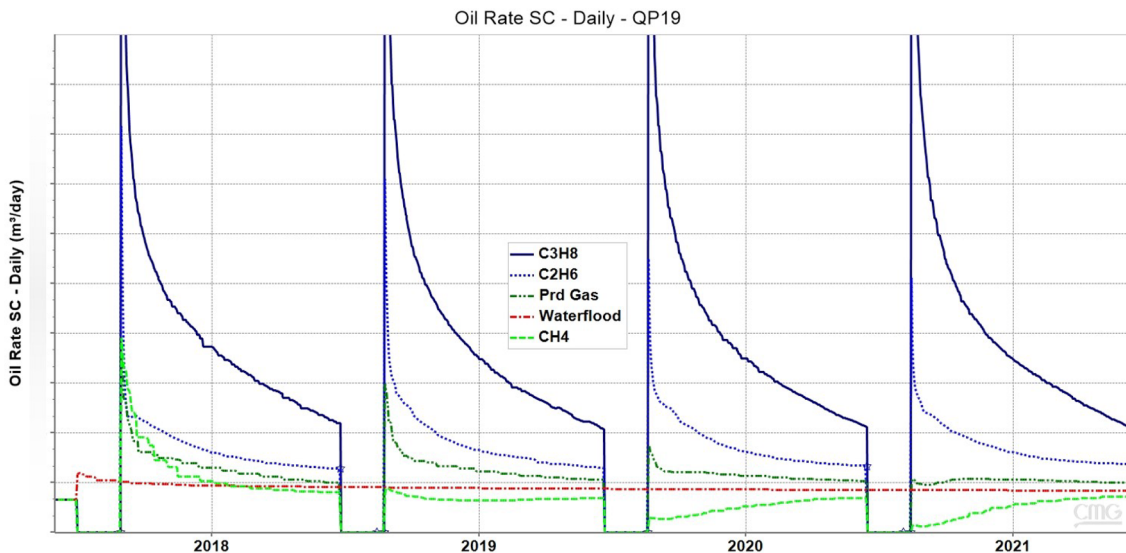

Fig. 15. Effect of the injectant's composition on oil rate.
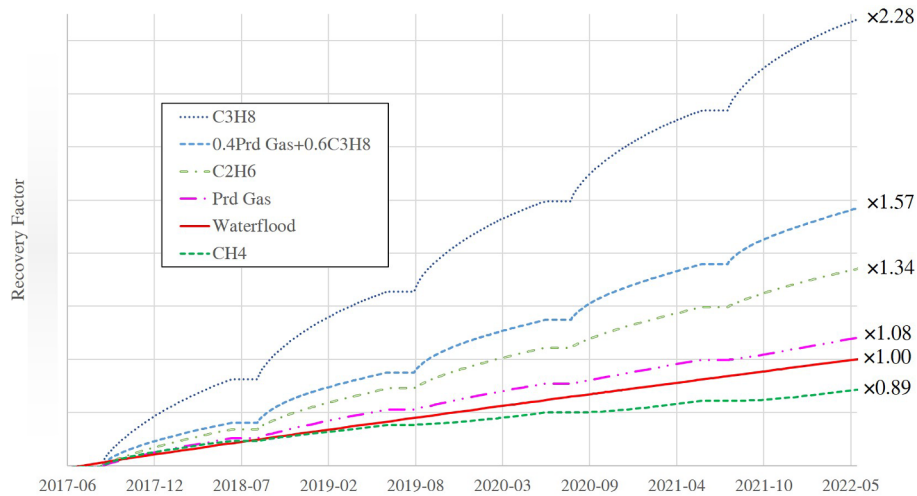
Fig. 16. Effect of the injectant's composition on RF.

tuned to match the water cut during waterflood. The conductivity and geometry for hydraulic fractures were kept the same as the base case. As shown in Fig. 24, the recovery factor curves with different fracture spacings almost overlapped with each other after re-history-matching. The difference between natural fracture spacing as 0.6 m and 8 m after C_3H_8 huff-n-puff was almost negligible, which implies that as long as the BHP and water cut could match the historical data, huff-n-puff performance is insensitive to the uncertainties in fracture spacing. But the difference of dual-porosity model and single-porosity model was significant. The single porosity model though under the same injection pressure had a much lower recovery factor than the dual-porosity model. C_3H_8 injection simulated by the single-porosity model only showed a minor improved oil recovery, which was consistent with the published work [43]. Physically, this was because dual-porosity model would lead to a much higher interacting area between injected gas in fractures and stranding oil in the matrix. Based on the value range of the fracture spacing [35–37], we could hence verify the technical feasibility of rich gas injection in Chang 6_3 with the dual-porosity compositional simulation, which is less time-consuming and more economically affordable compared with core flood or field pilots.

4. Conclusions

Ultra-low permeability Triassic formations, such as Chang 6_3, has become the new priority for developing the Ordos Basin. Due to the inefficiency of current waterflood, the feasibility of gas huff-n-puff in Chang 6_3 was investigated using a compositional modeling framework. An eight-component fluid characterization was established to fit the experimental data. A typical well pattern was selected for compositional simulation, whose key inputs were calibrated by matching the historical data. Huff-n-puff with various gases were simulated and compared with the waterflood scenario.

The simulation shows that the richer the injected gas, the higher the oil recovery. C_3H_8 injection achieves the best performance and increase
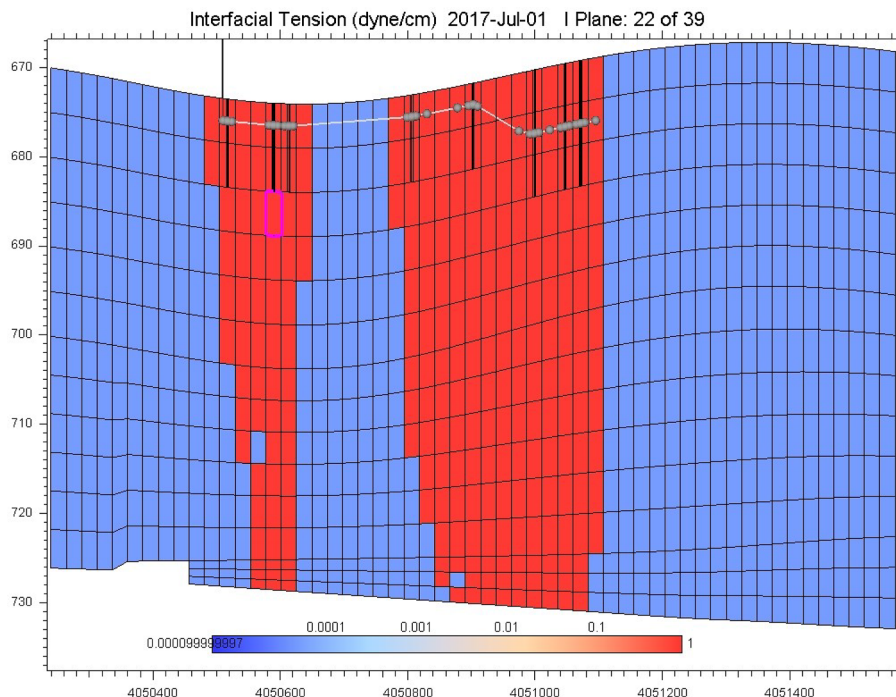

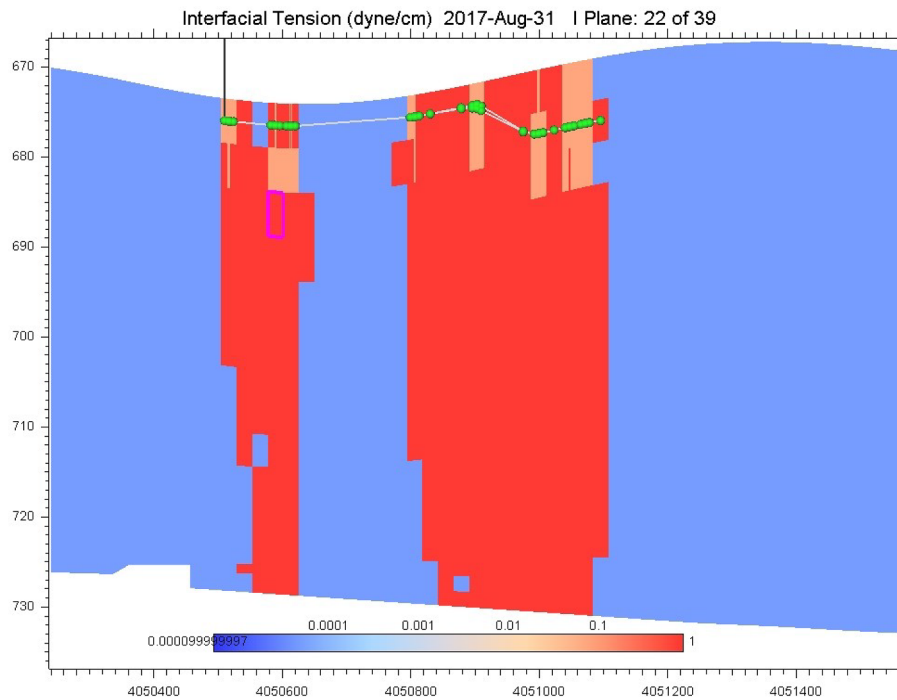**Fig. 17.** Map of calculated IFT in the J-K plane after primary depletion.

Fig. 18. Map of calculated IFT in the J-K plane after CH_4 injection.

the cumulative oil production by a factor of 2.28 after 5 cycles, then followed by C_2H_6 as 1.34, produced gas as 1.08.

Lean gas has a lower recovery factor than waterflood, because its MMP is close to the maximum allowable injection pressure, i.e., the minimum horizontal stress. Under the current well placement plan with the producer placed at the reservoir top, the miscible oil bank, which forms at the front of lean gas injection, would be displaced towards the reservoir bottom even out of the SRV, making lean gas injection

ineffective. However, the rich gas injection is compatible with such well placement design, as the miscible bank forms at the injection tail.

The simulation also shows increasing injection pressure will increase the recovery factor. Moreover, the leaner composition could be compensated by a higher injection pressure. Gas injection performance is also found to be dependent on injection time and soaking time after the sensitivity analysis.

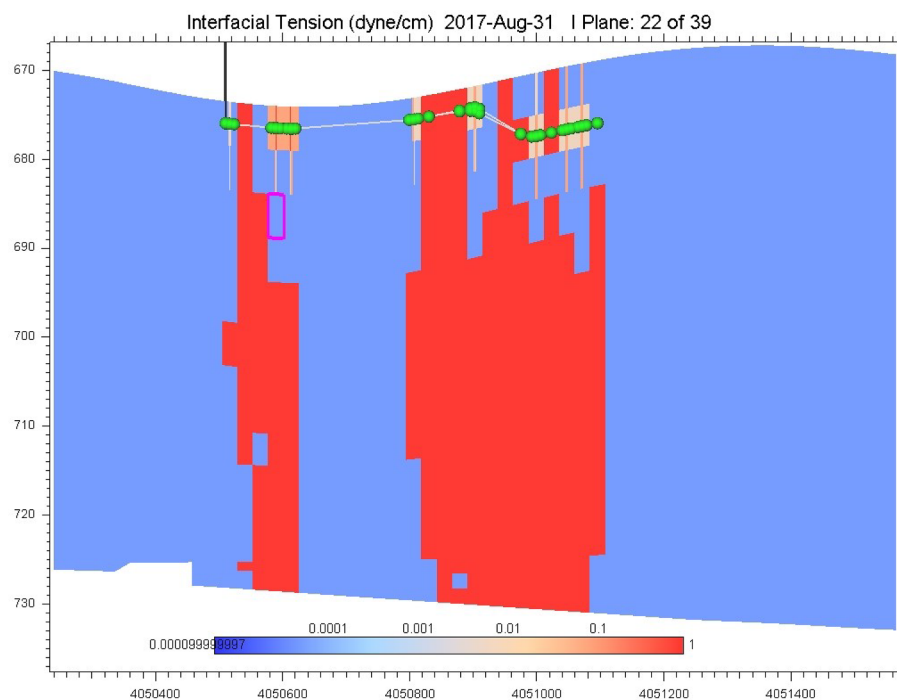Gas huff-n-puff performance is insensitive to the uncertainties in

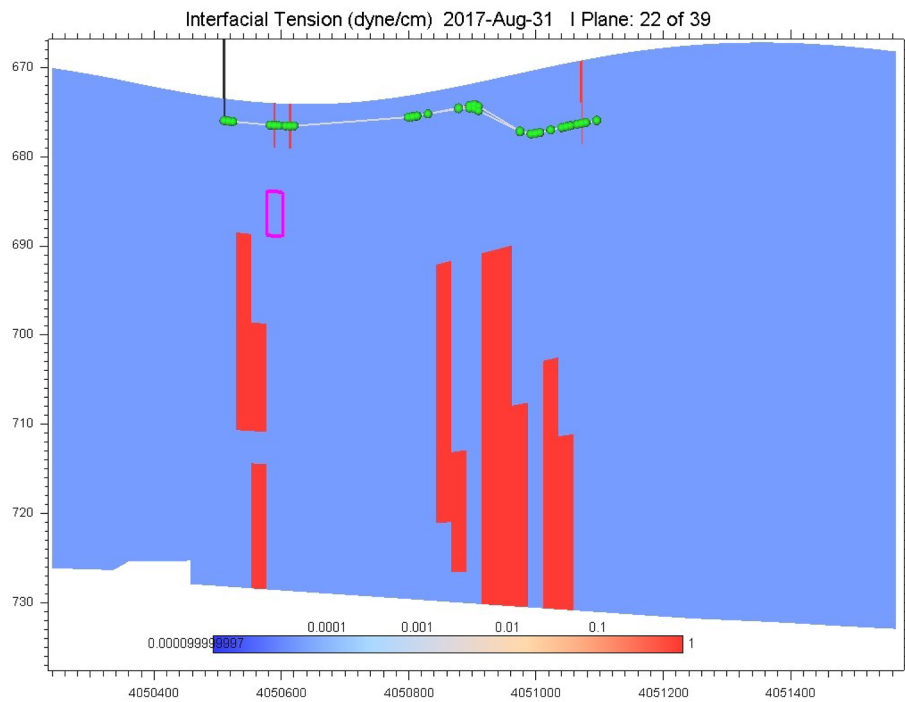**Fig. 19.** Map of calculated IFT in the J-K plane after the produced gas injection.

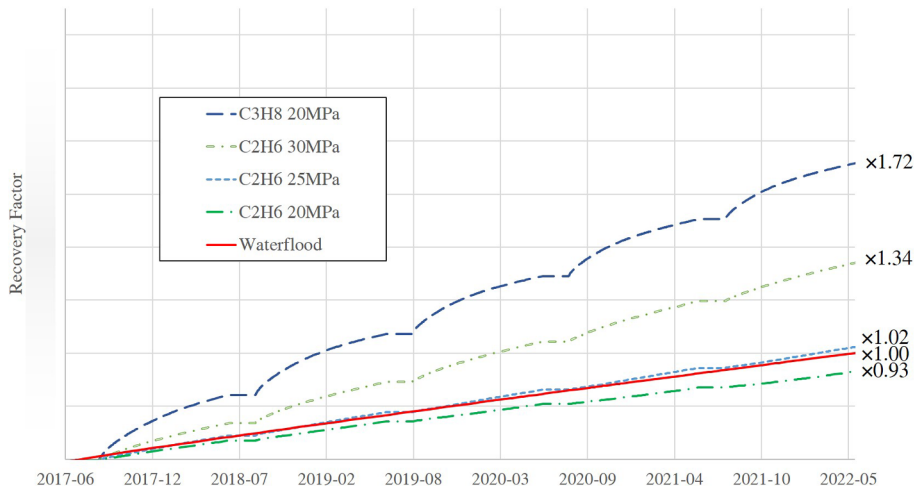**Fig. 20.** Map of calculated IFT in the J-K plane after C_3H_8 injection.

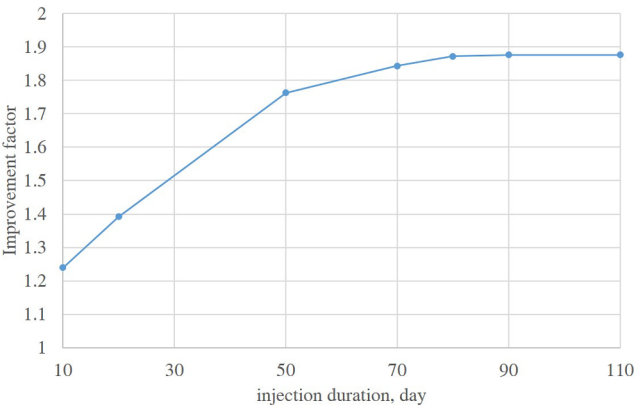**Fig. 21.** Effect of injection pressure on rich gas (C_2H_6) injection.

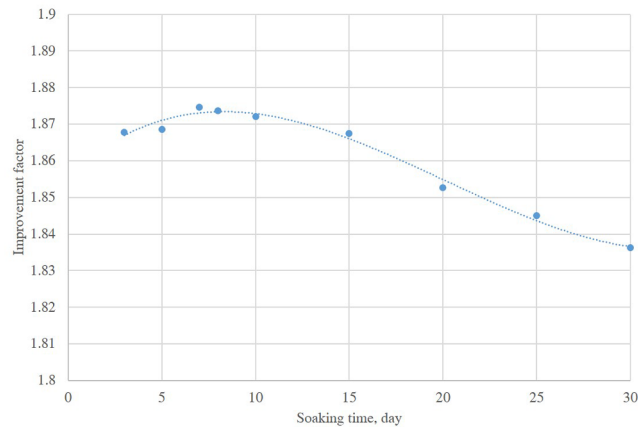**Fig. 22.** Impact of injection duration per cycle on C_2H_6 huff-n-puff.

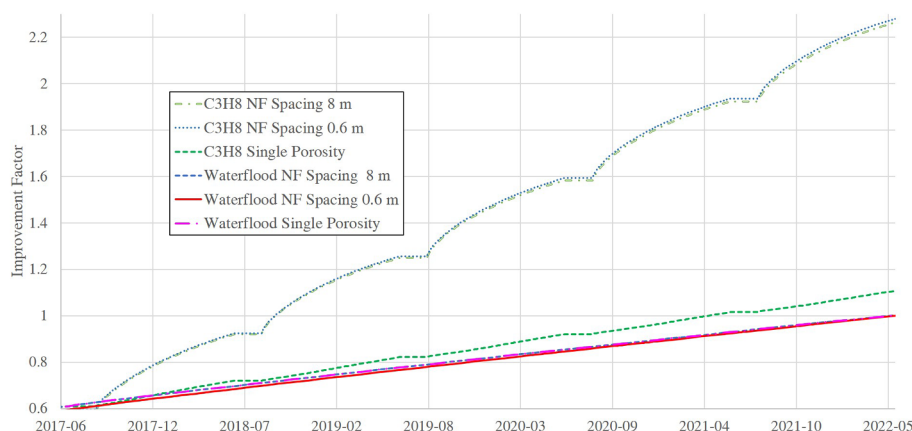**Fig. 23.** Impact of soaking time per cycle on C_2H_6 huff-n-puff.

Fig. 24. Impact of fracture spacing on C_3H_8 huff-n-puff.

fracture spacing as long as the BHP and water cut match the historical data. Using the fracture spacing data from the published work, we could verify the technical feasibility of rich gas injection in Chang 6_3 with the dual-porosity compositional simulation, which to the best of our knowledge, is the first time for this region.

5. Unit conversion factors

$$\text{atm} \times 101325 = \text{Pa}$$
$$\text{°C} + 273.15 = \text{K}$$
$$\text{cP} \times 0.001 = \text{Pa·s}$$
$$\text{dyn/cm} \times 0.001 = \text{N/m}$$
$$\text{in} \times 0.0254 = \text{m}$$
$$\text{mD} \times 9.869 \times 10^{-16} = \text{m}^2$$
$$\text{psi} \times 6894.757 = \text{Pa}.$$

CRediT authorship contribution statement

Ye Tian: Writing - original draft, Methodology. **Ozan Uzun:** Investigation. **Yizi Shen:** Writing - review & editing. **Zhengdong Lei:** Resources, Data curation. **Jiangru Yuan:** Project administration. **Jiaheng Chen:** Resources. **Hossein Kazemi:** Writing - review & editing, Conceptualization. **Yu-Shu Wu:** Funding acquisition, Supervision.

Declaration of Competing Interest

The authors declare that they have no known competing financial interests or personal relationships that could have appeared to influence the work reported in this paper.

References

[1] Liu X, Chang Y, Lu H, Chen B, Li J, Qi Y, Wang C. Optimizing fracture stimulation in low-permeability oil reservoirs in the ordos basin. SPE Asia pacific oil and gas conference and exhibition. Society of Petroleum Engineers; 2012.

[2] Yu H, Yang Z, Luo L, Liu J, Cheng S, Qu X, Lei Q, Lu J. Application of cumulative-in-situ-injection-production technology to supplement hydrocarbon recovery among fractured tight oil reservoirs: a case study in changqing oilfield, China. Fuel 2019;242:804–18.

[3] Shangguan Y, Zhang Y, Xiong W. The effect of physical property change on the water flooding development in changqing oilfield jurassic low permeability reservoir. Petroleum 2015;1:300–6.

[4] Teklu TW. Experimental and numerical study of carbon dioxide injection enhanced oil recovery in low-permeability reservoirs [Ph.D. thesis]. Colorado School of Mines; 2015.

[5] Wang L, Tian Y, Yu X, Wang C, Yao B, Wang S, Winterfeld PH, Wang X, Yang Z, Wang Y, Cui J, Wu Y-S. Advances in improved/enhanced oil recovery technologies for tight and shale reservoirs. Fuel 2017;210:425–45.

[6] Alvarez J, Schechter D. Altering wettability in bakken shale by surfactant additives and potential of improving oil recovery during injection of completion fluids. SPE improved oil recovery conference, society of petroleum engineers. 2016.

[7] Yang J, Wang X, Peng X, Du Z, Zeng F. Experimental studies on CO_2 foam performance in the tight cores. J Petrol Sci Eng 2019;175:1136–49.

[8] Wang M, Abeykoon GA, Argüelles-Vivas FJ, Okuno R. Ketone solvent as a wettability modifier for improved oil recovery from oil-wet porous media. Fuel 2019;258:116195.

[9] Alharthy N, Teklu TW, Kazemi H, Graves RM, Hawthorne SB, Braunberger J, Kurtoglu B. Enhanced oil recovery in liquid-rich shale reservoirs: laboratory to field. SPE Reserv Eval Eng 2018;21:137–59.

[10] Tian Y, Xiong Y, Wang L, Lei Z, Zhang Y, Yin X, Wu Y-S. A compositional model for gas injection ior/eor in tight oil reservoirs under coupled nanopore confinement and geomechanics effects. J Nat Gas Sci Eng 2019;71:102973.

[11] Hoffman TB, Reichhardt D. Quantitative evaluation of recovery mechanisms for huff-n-puff gas injection in unconventional reservoirs. Unconventional resources technology conference, unconventional resources technology conference. 2019.

[12] Abedini A, Torabi F. Oil recovery performance of immiscible and miscible CO_2) huff-and-puff processes. Energy Fuel 2014;28:774–84.

[13] Atan S, Ajayi A, Honarpour M, Turek E, Dillenbeck E, Mock C, Ahmadi M, Pereira C. The viability of gas injection eor in eagle ford shale reservoirs. SPE annual technical conference and exhibition. Society of Petroleum Engineers; 2018.

[14] Hoffman TB. Huff-n-puff gas injection pilot projects in the eagle ford. SPE Canada unconventional resources conference. Society of Petroleum Engineers; 2018.

[15] Zhang C, Tian Y, Shen Y, Yao B, Wu Y-S. Simulation of high water-cut in tight oil reservoirs during cyclic gas injection. SPE liquids-rich basins conference-North America. Society of Petroleum Engineers; 2019.

[16] Xin Y. Evaluating of the effect of water injection development in Yuan 284 well area in Longdong area (in Chinese) [Master's thesis]. Xi'an Shiyou University; 2019.

[17] Shi T. The Study on the Micro-pore Structure and Percolation Characteristics of Yanchang Formation Chang6 Reservoir in Huaqing Area [Ph.D. thesis]. Northwest University; 2012.

[18] Ran X. Advanced water injection for low permeability reservoirs: theory and practice. Gulf: Professional Publishing; 2013.

[19] Dong Y. Evaluating of Development effects of Horizontal well in Yuan 284 Region, Huaqing oilfield (in Chinese) [Master's thesis]. Xi'an Shiyou University; 2015.

[20] Zhao J, Fan J, He Y, Yang Z, Gao W, Gao W. Optimization of horizontal well injection-production parameters for ultra-low permeable–tight oil production: a case from changqing oilfield, ordos basin, nw china. Petrol Explor Dev 2015;42:74–82.

[21] Hu D. Study on optimization of combined imbibition and displacement development technology for ultralow permeability reservoir (in Chinese) [Master's thesis]. China University of Petroleum; 2018.

[22] CMG, WinProp user's guide. Computer Modeling Group Ltd.: Calgary, Canada; 2018.

[23] Robinson DB, Peng D-Y. The characterization of the heptanes and heavier fractions for the GPA Peng-Robinson programs. Gas Processors Association; 1978.

[24] Zudkevitch D, Joffe J. Correlation and prediction of vapor-liquid equilibria with the redlich-kwong equation of state. AIChE J 1970;16:112–9.

[25] Khan SA. An expert system to aid in compositional simulation of miscible gas flooding [Ph.D. thesis]. University of Texas at Austin; 1992.

[26] Péneloux A, Rauzy E, Fréze R. A consistent correction for redlich-kwong-soave volumes. Fluid Phase Equilibria 1982;8:7–23.

[27] Jossi JA, Stiel LI, Thodos G. The viscosity of pure substances in the dense gaseous and liquid phases. AIChE J 1962;8:59–63.

[28] Jhaveri BS, Youngren GK. Three-parameter modification of the peng-robinson equation of state to improve volumetric predictions. SPE Reserv Eng 1988;3:1033–40.

[29] Cho Y, Ozkan E, Apaydin OG. Pressure-dependent natural-fracture permeability in shale and its effect on shale-gas well production. SPE Reserv Eval Eng 2013;16:216–28.

[30] Zhu S-Y, Du Z-M, Li C-L, Salmachi A, Peng X-L, Wang C-W, Yue P, Deng P. A semi-analytical model for pressure-dependent permeability of tight sandstone reservoirs. Transp Porous Med 2018;122:235–52.

[31] Teklu TW, Zhou Z, Li X, Abass H. Cyclic permeability and porosity hysteresis in mudrocks–experimental study. 50th US rock mechanics/geomechanics symposium. American Rock Mechanics Association; 2016.

[32] Abdallah W, Buckley JS, Carnegie A, Edwards J, Herold B, Fordham E, Graue A, Habashy T, Seleznev N, Signer C, Hussain H, Montaron B, Ziauddin M. Fundamentals of wettability. Schlumberger Oilfield Rev 2007;38:44–61.

[33] Botto J. Effects of surface mineralogy and roughness on CO2 wettability of the Mount Simon sandstone; implications for predicting CO2 storage capacity and pore scale transport [Master's thesis]. University of Texas at Austin; 2016.

[34] CMG. GEM user's guide. Computer Modeling Group Ltd.: Calgary, Canada; 2018.

[35] Zeng L, Li X-Y. Fractures in sandstone reservoirs with ultra-low permeability: a case study of the upper triassic yanchang formation in the ordos basin, china. AAPG Bull 2009;93:461–77.

[36] Liu G. Research on fracture developing characteristics of Chang 6 reservoir, Yangchang group in Huaqing area, Changqing petroleum field (in Chinese) [Master's thesis]. Lanzhou University; 2010.

[37] Liu G, Huang C, Zhou X, Zhang L, Pan Y. Quantitative evaluation of fracture development in triassic yanchang formation, ordos basin, nw china. Petrol Explor Dev 2015;42:486–96.

[38] Katz D, Monroe R, Trainer R. Surface tension of crude oils containing dissolved gases. Pet Technol 1943;6:1–10.

[39] Song C, Yang D. Experimental and numerical evaluation of CO_2 huff-n-puff processes in bakken formation. Fuel 2017;190:145–62.

[40] Hoteit H. Modeling diffusion and gas–oil mass transfer in fractured reservoirs. J Petrol Sci Eng 2013;105:1–17.

[41] Coats KH. Implicit compositional simulation of single-porosity and dual-porosity reservoirs. SPE symposium on reservoir simulation. Society of Petroleum Engineers; 1989.

[42] Hoteit H, Firoozabadi A. Numerical modeling of diffusion in fractured media for gas-injection and-recycling schemes. SPE J 2009;14:323–37.

[43] Carlsen M, Whitson C, Dahouk MM, Younus B, Yusra I, Kerr E, Nohavitza J, Thuesen M, Drozd J, Ambrose R. Compositional tracking of a huff-n-puff project in the eagle ford. Unconventional resources technology conference. 2019.